International Journal of Plasticity 159 (2022) 103482

Contents lists available at ScienceDirect

International Journal of Plasticity

journal homepage: www.elsevier.com/locate/ijplas

Quantitative analysis of hetero-deformation induced strengthening in heterogeneous grain structure

T.H. Chou [a,e], W.P. Li [a,*], H.W. Chang [b], X.H. Du [c], W.S. Chuang [a,d], T. Yang [a,e,*], Y.T. Zhu [a], J.C. Huang [a,b,*]

[a] Department of Materials Science and Engineering; Mechanical Behavior Division of Shenyang National Laboratory for Materials Science; Hong Kong Institute for Advanced Study, City University of Hong Kong, Kowloon, Hong Kong

[b] Department of Materials and Optoelectronic Science No data was used for the research described in the article, National Sun Yat-Sen University, Kaohsiung, Taiwan

[c] School of Materials Science and Engineering, Shenyang Aerospace University, Shenyang, China

[d] Metal Processing R&D Department, Metal Industries Research & Development Centre, Kaohsiung, Taiwan

[e] Hong Kong Branch of National Precious Metals Material Engineering Research Centre (NPMM), City University of Hong Kong, Hong Kong

ARTICLE INFO

Keywords:
HDI strengthening
Dislocation pileup
Hetero-boundary affected region
Medium entropy alloy
Heterogeneous grain structure
Heterostructured materials

ABSTRACT

A single-phase bimodal grain structure is considered to develop a physical model to quantify hetero-deformation induced (HDI) strengthening at the yield point, which cannot be simply predicted by the conventional rule-of-mixtures using the Hall-Petch equation. Based on the classic theory of single-ended continuum dislocation pileup, the modified model parameterizes the effective width of hetero-boundary affected region (Hbar) as well as the contribution of HDI stress to 0.2% proof stress. To further verify the model equations, the equimolar CoCrNi medium entropy alloy was selected as a model material. The heterogeneous grain structure (HGS) was introduced via thermal-mechanical treatment, and statistical analysis of microstructure was performed by means of electron backscattered diffraction. By substituting derived parameters, our model can predict theoretical values of the yield stress and the width of Hbar, both comparable to the experimental value from tensile testing, as well as previous experimental observations. The reasonable agreements can not only prove the validity of the current modified model, but also bring out physical explanations for the extra strengthening in heterostructured materials.

1. Introduction

Pursuing strong and yet ductile materials has long been a priority for structural materials scientists, but the higher strength usually means the sacrifice of the ductility and toughness. Recent developments on materials with heterostructures have drawn extensive attention due to the great potential to overcome such strength-ductility trade-off. An early research, in 2002, revealed the importance of the heterogeneous grain structure on mechanical properties and presented a superb combination of strength and ductility in a pure copper (Wang et al., 2002). After that, additional efforts were recently put into other materials, such as steels (Niu et al., 2022; Yang et al., 2016b; Zhong et al., 2022; Zou et al., 2022), titanium alloys (Gao et al., 2018; Shin et al., 2019; Wu et al., 2015; Zhang et al., 2021), and multi-principal element alloys (MPEAs), known as high/medium entropy alloys (HEAs/MEAs) (Fan et al., 2022; Hasan

* Corresponding authors.
E-mail addresses: wanpengli2@cityu.edu.hk (W.P. Li), taoyang6@cityu.edu.hk (T. Yang), chihuang@cityu.edu.hk (J.C. Huang).

https://doi.org/10.1016/j.ijplas.2022.103482
Received 30 August 2022; Received in revised form 12 November 2022;
Available online 16 November 2022

Nomenclature

ε_t	total elongation
ε_u	uniform elongation
μ	shear modulus
ν	Poisson's ratio
σ_a	applied stress
σ_b	back stress
σ_{CG}	yield stress of coarse grains
$\sigma_{CG.b}$	yield stress of those coarse grains adjacent to the region of fine grains
σ_c	critical stress
σ_e	effective stress
σ_{FG}	yield stress of fine grains
σ_{HDI}	hetero-deformation induced stress
σ_{tip}	tip stress
σ_u	ultimate tensile stress
σ_{uy}	unloading yield stress
σ_{ry}	reloading yield stress
σ_y	yield stress
σ_0	friction stress
$\sigma_{0,NG}$	friction stress of nanograins
$\sigma_p(x)$	stress at x resulting from interdislocation interactions
τ_a	applied resolved shear stress
b	Burgers vector
d	mean grain size
E	Young's modulus
f_{CG}	area fraction of coarse grains
$f_{CG,b}$	area fraction of those coarse grains adjacent to the region of fine grains
f_{FG}	area fraction of fine grains
f_{rc}	fraction of recrystallized grain
f_{urc}	fraction of unrecrystallized grain
k	Hall-Petch constant
k_{NG}	Hall-Petch constant of nanograins
l	length of a dislocation pileup
l_{Hbar}	width of hetero-boundary affected region
l_0	the end of dislocation pileup
M	Taylor factor
N	number of dislocations
N_{Hbar}	number of dislocations within hetero-boundary affected region
$n(x)$	dislocation density at x
CG	coarse grain
FG	fine grain
GND	geometrically necessary dislocation
GOS	grain orientation spread
Hbar	hetero-boundary affected region
HEA	high entropy alloy
HDI	hetero-deformation induced
HGS	heterogeneous grain structure
HS	heterostructured
IAZ	interface-affected zone
LUR	loading-unloading-reloading
MEA	medium entropy alloy
MPEA	multi-principal element alloy
ROM	rule-of-mixtures
SFE	stacking fault energy
TMT	thermo-mechanical treatment

et al., 2019; He et al., 2021; He et al., 2021; Li et al., 2021; Wu et al., 2019; Xiong et al., 2020; Yang et al., 2018). Besides, various heterostructures introduced by different strategies were systematically reviewed (Misra et al., 2021; Sathiyamoorthi and Kim, 2022; Wu and Fan, 2020; Zhu et al., 2021) and classified as follows: gradient grain structures (Hasan et al., 2019; Lu, 2014; Wang et al., 2020; Wu et al., 2014), layered structures (Huang et al., 2018; Ma et al., 2016; Wang et al., 2019; Wang et al., 2018;), harmonic structures (Park et al., 2018; Sawangrat et al., 2014; Zhang et al., 2014), multi-phase structures (Gao et al., 2019; Gao et al., 2018; Xiong et al., 2020; Yang et al., 2016b), multi-modal grain structures (Fan et al., 2022; Li et al., 2021; Liu et al., 2022; Niu et al., 2022; Shin et al., 2019; Shukla et al., 2018; Wang et al., 2002; Wu et al., 2019; Wu et al., 2015; Yang et al., 2018; Zhang et al., 2019), etc. Materials featuring these heterostructures can be further identified as heterostructured (HS) materials. Since such a surprising combination of strength and ductility in the above HS materials cannot be rationalized by traditional strengthening mechanisms or rule-of-mixtures (ROM) alone (Kim et al., 2019; Lai et al., 2022; Li et al., 2020; Li et al., 2021; Slone et al., 2019; Wang et al., 2019; Wu et al., 2014), a concept based on the long-range stress, hetero-deformation induced (HDI) strengthening, is raised to illuminate the extra strengthening and strain hardening effect (Yang et al., 2016a; Zhu and Wu, 2019).

The main figure behind the HDI strengthening is the difference in strength between the soft and hard zones in an HS material. The concept was firstly named and summarized by Zhu and Wu (Zhu and Wu, 2019). In the early stage of deformation (upon yielding), the soft zones start to plastically deform while the hard zones remain elastic, resulting in geometrically necessary dislocations (GNDs) to pile up against the boundary/interface between two zones to accommodate the strain gradient in the soft zone. The generated GNDs near the boundary/interface exert a long-range back stress, in the opposite direction against applied shear stress, which strengthens the soft zone, and finally, increases the global yield strength. Meanwhile, the hard zone will sustain a reaction stress, forward stress, at the tip of the pileup in the same direction as applied shear stress. As the HS material yields, i.e., both soft and hard zones deform plastically, the back stress and forward stress develop in these two zones respectively to realize the strain and stress partitioning at the boundary/interface. Then, the coupled effect of these two stresses during the whole deformation is defined as HDI stress; the extra hardening is further called HDI hardening.

In practice, the contribution of the HDI stress to the total flow stress is usually estimated from the loading-unloading-reloading (LUR) tensile curve (Yang et al., 2016a; Yang et al., 2016b); however, the local interactions between back stress and forward stress still remain unverified. More efforts on either experimental verification or theoretical modeling are needed to reveal the details of the strengthening mechanism. To address this issue, materials with single-phase grain structure are perhaps the simplest types of heterostructures to beginning with. In addition, it has been argued that GND pileups can be promoted in materials with low stacking fault energies (SFEs) because of the nature of easier planar slip deformation mechanism (Zhu et al., 2021), making HDI strengthening more effective. Moreover, current investigations suggested that, in comparison to conventional alloys, single-phase equimolar MPEAs with low SFEs exhibit not only larger spacings between partial dislocations but also relatively low probabilities of cross slip (Bouaziz et al., 2021; Park et al., 2021), which could further arise profound HDI strengthening. Therefore, such kinds of materials can be selected for fundamental studies of HDI strengthening.

According to the scenario of HDI strengthening discussed above, it has been recently reported that the strength and ductility of

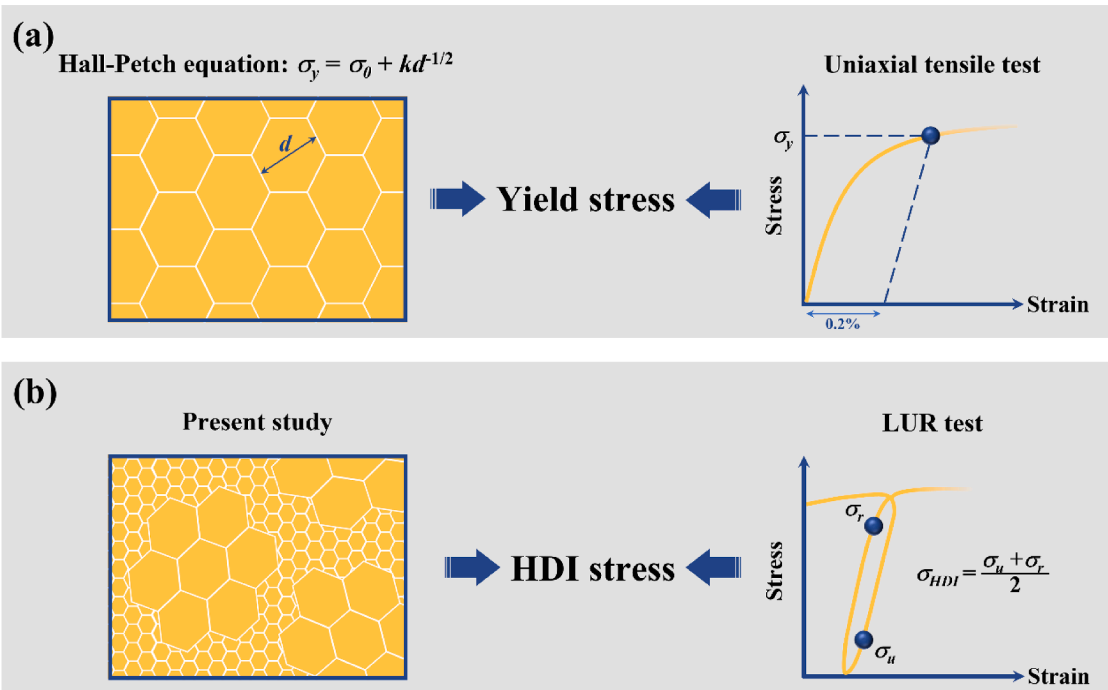

Fig. 1. Schematic illustration of (a) yield stress and (b) HDI stress determined from theoretical prediction and experiments, respectively.

equimolar CoCrNi MEA with a single FCC structure and low SFE could be increased simultaneously by introducing partial recrystallization as a heterogeneous grain structure (HGS) (Lu et al., 2020; Sathiyamoorthi et al., 2019; Sathiyamoorthi et al., 2018; Slone et al., 2019; Yang et al., 2018). After the thermo-mechanical treatment (TMT) was applied, an excellent yield strength of ~1.1 GPa combined with a decent uniform strain of ~22% was achieved in the partially recrystallized CoCrNi MEA consisting of three levels of grain sizes (Yang et al., 2018). Later, heavily cold-rolled CoCrNi MEA followed by various annealing conditions was systematically studied (Lu et al., 2020; Sathiyamoorthi et al., 2019; Slone et al., 2019). The mechanical properties of the alloys with homogeneous grain structures were compared to that with HGS in response to different recrystallization fractions. In these investigations, unrecrystallized/deformed grains and recrystallized fine grains (FGs) act as hard zones, while recrystallized coarse grains (CGs) represent soft zones; as expected, HDI stress is proven to play a pivotal role of additional hardening in the flow stress by the LUR testing. Therefore, the equimolar CoCrNi MEA with HGS can be an ideal prototype to study HDI strengthening in detail.

Apart from traditional strengthening mechanisms, e.g., solid-solution strengthening, grain boundary strengthening, strain hardening, precipitation hardening, and dispersion strengthening, a theoretical way to quantify HDI strengthening is still lacking. Here we aim to develop a model based on classic theories of dislocations, in contrast to macroscopic LUR testing, to quantify important characteristics of HDI stress, especially in the early elasto-plastic deformation stage. Then, the modeling results are applied to conjugate the HGS of equimolar CoCrNi introduced by TMT similar to methods in literature. It is shown that the model gives reasonable values of critical parameters in material mechanics, including the length of pileup against hard zones, that is, interface-affected zone (IAZ), which was later defined as the hetero-boundary affected region (Hbar). As the Hall-Petch relationship is commonly used to estimate the yield stress according to the grain size of the homogeneous grain structure, our model can be expected to predict the contribution of HDI stress in a specific HGS as well as the global yield stress, coupled with the Hall-Petch relationship and the ROM.

2. Model development

To relate microstructure (or grain size) to mechanical response (yield strength) like the Hall-Petch relationship, critical progresses in dislocation modeling is briefly reviewed first, followed by developing a modified model in consideration of HDI strengthening. The yield strength, 0.2% proof stress, of a homogeneous polycrystalline material is universally determined by the tensile test, and the Hall-Petch relationship is well-known for predicting its value, linearly proportional to the reciprocal square root of grain size, as illustrated in Fig. 1(a). Likewise, the motivation is to characterize the HDI stress, determined from the LUR testing thus far, in a single-phase material featuring HGS, as illustrated in Fig. 1(b).

2.1. Single-ended dislocation pileup

It has been proved that the Hall-Petch relationship has wide-range applications over the past decades since it was proposed by Hall in 1951 (Hall, 1951) and Petch in 1953 (Petch, 1953). According to Hall's experiment on mild steel, the yield stress (σ_y) can be related to the mean grain size (d), and expressed by an empirical function:

$$\sigma_y = \sigma_0 + kd^{-1/2} \tag{1}$$

where σ_0 is the friction stress, and k is the Hall-Petch constant or slope. The original explanation of the mechanism involved dislocation pileups against the grain boundary using the 'dislocation clogging' mechanism (Cottrell and Bilby, 1949). Under an applied stress, the grain boundary acts as an effective barrier to impede the movement of dislocations, resulting in dislocation pileups and the stress concentration near the boundary. When the stress concentration reaches a critical value, i.e., dislocations are able to pass through the grain boundary, yielding of the material is to take place. Then the grain boundary density or grain size is regarded as the main factor to evaluate the yield stress, because decreasing the grain size alleviates dislocation pileups inside the material, requiring a higher applied stress to make dislocations move across grain boundaries. This strengthening mechanism is generally known as the grain-boundary or

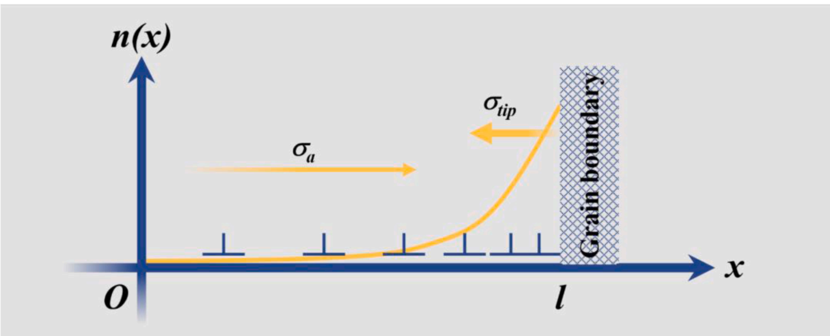

Fig. 2. Schematic illustration of a single-ended dislocation pileup against the grain boundary under the applied stress (σ_a). The dislocation density ($n(x)$) increases along the pileup length of l, as described by Eq. (4). The tip stress (σ_{tip}), coming after the pileup, acts on the leading dislocations as a local reaction stress.

grain-refinement strengthening.

In the wake of the Hall-Petch relation, a lot of experiments and theoretical modeling were performed to either examine the reliability of the Hall-Petch relationship or explain its physical meaning from the viewpoint of dislocation theory. To study the mechanism of dislocation pileups, there are two approaches, namely continuum (Eshelby, 1949) and discrete (Eshelby et al., 1951) models, both of which were worked out firstly by Eshelby in 1949 and 1951. In Hall's study (Hall, 1951), Eq. (1) was initially rationalized using the discrete dislocation pileup model, which provides more intuitive derivation when only few dislocations in pileups are considered; otherwise, it may contain possible sources of errors (Hirth et al., 1983). By comparison, the continuum model, in consideration of the continuous distribution of dislocations in the pileup, has an advantage in solving the pileup problem using the infinitesimal Burgers vector, especially for a large group of dislocations. Even though an unreasonable value of stress field could yield when the distance from the pileup is much larger than the inter-dislocation spacing, the merit of simpler mathematical treatments makes the continuum model more favorable to complex cases, such as the Peierls-Nabarro model and the evolution of partial dislocations. Numerical solutions for both models had been first reviewed by Li and Chou (Li and Chou, 1970), and later summarized in *Theory of Dislocations* (Hirth et al., 1983). Derivations presented below start with the original Eshelby-Frank-Nabarro problem, solved by Leibfried (Leibfried, 1951) and Head and Louat (Head and Louat, 1955), followed by the continuum single-ended pileup model.

Consider a row of edge dislocations, with a length of l, piles up against the grain boundary due to the applied resolved shear stress ($\tau_a = \sigma_a/M$), where M is Taylor factor and σ_a is the applied stress, as illustrated in Fig. 2. The dislocation density is defined as (Hirth et al., 1983):

$$n(x) = \frac{1}{b}\frac{db}{dx} \tag{2}$$

where b is the Burgers vector. The equilibrium condition can be satisfied without the presence of Peach-Koehler force on the pileup, i.e., σ_a acting on each dislocation is balanced by the net interaction force experienced by other dislocations. That is (Hirth et al., 1983),

$$(\sigma_a - \sigma_0)b = \frac{M\mu b^2}{2\pi(1-\nu)}\int_0^l \frac{n(x')}{x-x'}dx' \quad (0 \le x \le l) \tag{3}$$

where μ is the shear modulus, ν is the Poisson's ratio, and the integral is determined by its principal value. Eq. (3) can be solved using the Hilbert transformation (Head and Louat, 1955; Leibfried, 1951). Here, we directly adopt the solution to $n(x)$:

$$n(x) = \frac{2(1-\nu)(\sigma_a - \sigma_0)}{M\mu b}\frac{(l-x)^{1/2}}{x^{1/2}} \tag{4}$$

and the number of dislocations in the pileup is

$$N = \int_0^l n(x)dx = \frac{\pi(1-\nu)(\sigma_a - \sigma_0)l}{M\mu b} \ . \tag{5}$$

The accumulated dislocations near the grain boundary will result in a concentrated stress at the tip of the pileup (tip stress), which can be obtained from the multiplied stress as follows (Hirth et al., 1983; Li and Chou, 1970):

$$\sigma_{tip} = N(\sigma_a - \sigma_0) \tag{6}$$

This local reaction stress, several times higher than σ_a, impedes further movement of leading dislocations across the grain boundary to propagate plastic deformation. Thus, yielding will occur when the σ_{tip} reaches a critical value (σ^*_{tip}). By applying conditions of $\sigma_{tip} = \sigma^*_{tip}$ and $l = d$, substituting Eq. (5) into Eq. (6) can give

$$\sigma_a = \sigma_y = \sigma_0 + \sqrt{\frac{M\mu b\sigma^*_{tip}}{\pi(1-\nu)}}d^{-1/2} \tag{7}$$

where the square root term corresponds to k in Eq. (1). As a result, the general form of the Hall-Petch equation is derived from single-ended pileup model, as shown in Eq. (7).

2.2. Characterizing HDI strengthening at yield point

Before constructing the model, it is necessary to look more deeply into the process of HDI hardening and sketch out the main idea. When the tensile testing is conducted on the material with HGS, inhomogeneous deformation induces back stress in soft zones (CGs) and the forward stress in hard zones (FGs), defined as HDI strengthening, enhancing the yield strength and strain hardening. During elasto-plastic deformation, forward stresses are not high enough to plastically deform the hard zone yet, we will only need to focus on the back stress before yielding.

Upon yielding point, at 0.2% offset strain, soft zones deform plastically while hard zones remain elastic, in consequence, GNDs generate in the former to sustain plastic strain. However, soft zones are surrounded by hard zones, impeding free movements of GNDs across the zone boundaries (interfaces) in this situation. As a result, GNDs pile up against the interface to accommodate the strain gradient. Furthermore, piled-up GNDs exert back stress inside the soft zone opposite to the applied stress, which hinders the following emission of GNDs from the Frank-Reed source. Such difficulty in dislocation movements is similar to the classic mechanism of Hall-Petch strengthening, and makes soft zones appear stronger. Finally, the global yield stress increases in response to the whole microscale process. Since the hard zones remain elastic at this stage, the only contribution to HDI hardening would mostly rely on the back stress in soft zones. In other words, the long-range back stress (σ_b) can be effectively seen as HDI stress (σ_{HDI}) at the yield point of the HGS material.

To build up the modified model for HGS materials, there are two additional conditions that need to be introduced to the classic continuum analysis of single-ended dislocation pileup: (1) the effective length of dislocation pileups (the width of Hbar); (2) the difference in strength between two zones relative to two grains with similar sizes. For the first condition, the influence of dislocation source is applied to the pileup, while the standard continuum theory is referred to as a source-independent theory. This can be achieved by employing Friedman and Chrzan's derivation (Friedman and Chrzan, 1998). And the second condition is assumed that the interface between two zones can more effectively hinder pileups in CGs from moving into FGs, owing to the nature of a higher yield strength of FGs than that of CGs. These two conditions will be considered, in sequence, in the following derivation.

Again, a row of edge dislocations piles up in a CG with a grain size of d_{CG} under the similar circumstance of Fig. 2; however, the end of dislocation pileup (l_0) is additionally considered, and the grain boundary is replaced by a specific interface between a CG and FGs, as illustrated in Fig. 3. It is assumed that dislocations are emitted from O, the left boundary, and stocked in the vicinity of the interface, denoted as Hbar. The width of Hbar (l_{Hbar}) is exactly the effective range of the dislocation pileup, extending from the right boundary, $x = d_{CG}$, to somewhere $n(x)$ approaches to 0, $x = l_0$, as indicated in Fig. 3. Thus,

$$l_{Hbar} = d_{CG} - l_0 \ . \tag{8}$$

Considering the presence of σ_a, Eq. (3) can be rewritten as

$$(\sigma_a - \sigma_0)b = \frac{M\mu b^2}{2\pi(1-\nu)} \int_{l_0}^{d_{CG}} \frac{n(x')}{x - x'} dx' \tag{9}$$

where all physical meanings of symbols have been defined in the previous discussion. The dislocation density ($n(x)$) can be solved as

$$n(x) = \frac{2(1-\nu)(\sigma_a - \sigma_0)}{M\mu b} \frac{(x - l_0)^{1/2}}{(d_{CG} - x)^{1/2}} \tag{10}$$

which is depicted by the yellow line in CG of Fig. 3. Then the integral is performed on Eq. (10) to give the number of dislocations within Hbar (N_{Hbar}):

$$N_{Hbar} = \int_{l_0}^{d_{CG}} n(x)dx = \frac{\pi(1-\nu)(\sigma_a - \sigma_0)(d_{CG} - l_0)}{M\mu b} \ . \tag{11}$$

To further consider the equilibrium upon yielding, σ_a is expected to be locally elevated as high as the yield stress of FGs (σ_{FG}) in Hbar. Since the CG is surrounded by FGs with a mean grain size of d_{FG}, as shown in the right side of Fig. 3, it is reasonable to view the interface as the grain boundary of FG to hinder the further movement of pileup in CG until σ_a increases to σ_{FG}. Hence, by the Hall-Petch equation, we have

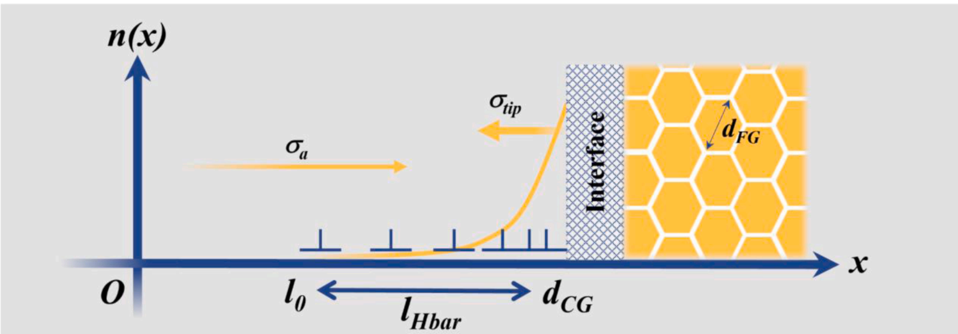

Fig. 3. Schematic illustration of a single-ended dislocation pileup against the interface between a CG and FGs under the σ_a within a CG. The $n(x)$ increases along the pileup length of l_{Hbar}, from d_{CG} to l_0, as predicted by Eq. (10). The σ_{tip}, coming after the pileup, acts on the leading dislocations as a local reaction stress.

$$N_{Hbar} = \frac{\pi(1-\nu)kd_{FG}^{-1/2}}{M\mu b}(d_{CG} - l_0) \tag{12}$$

Substituting Eq. (12) into Eq. (11) gives

$$N_{Hbar} = \frac{\pi(1-\nu)kd_{FG}^{-1/2}}{M\mu b}(d_{CG} - l_0) \tag{13}$$

or, in the expression of Eq. (8),

$$N_{Hbar} = \frac{\pi(1-\nu)kd_{FG}^{-1/2}}{M\mu b} l_{Hbar} \ . \tag{14}$$

So far, except for l_0, parameters in the above equations can be feasibly determined from either references or experiments, so the next step is to express l_0 in a solvable way. This can be realized by revealing the sum of stress at position x, which is

$$\sigma(x) = \sigma_a + \sigma_p(x) \tag{15}$$

where $\sigma_p(x)$ is the stress at x resulting from interdislocation interactions. Refer to previous solutions (Friedman and Chrzan, 1998; Hirth et al., 1983), $\sigma_p(x)$ can be further expressed as

$$\sigma_p(x) = -\sigma_a\left(1 - \sqrt{\frac{l_0 - x}{d_{CG} - x}}\right) \ . \tag{16}$$

And considering the condition of

$$\sigma(x=0) = \sigma_c \tag{17}$$

where σ_c is the critical stress to generate a dislocation from the dislocation source (Mott, 1952), for example, grain boundary ledge at O here, experienced by σ_a (Murr, 2016). In the elasto-plastic deformation stage, CGs presumably start to deform plastically, so the critical stress to activate dislocation can be equivalent to σ_{CG}. Then, l_0 can be solved by substituting Eqs. (12) and (16) into Eq. (15), and introducing the boundary condition of Eq. (17). That is

$$l_0 = \left(\frac{\sigma_{CG}}{\sigma_{FG}}\right)^2 d_{CG} \tag{18}$$

and l_{Hbar} in Eq. (8) will be

$$l_{Hbar} = \left[1 - \left(\frac{\sigma_{CG}}{\sigma_{FG}}\right)^2\right] d_{CG} \ . \tag{19}$$

Therefore, N_{Hbar} in Eq. (14), in combination with Eq. (19), can be determined for calculating σ_{tip} as follows:

$$N_{Hbar} = \frac{\pi(1-\nu)kd_{FG}^{-1/2}}{M\mu b}\left[1 - \left(\frac{\sigma_{CG}}{\sigma_{FG}}\right)^2\right] d_{CG} \tag{20}$$

and

$$\sigma_{tip} = N_{Hbar}(\sigma_a - \sigma_0) = \frac{\pi(1-\nu)k^2 d_{CG}}{M\mu b d_{FG}}\left[1 - \left(\frac{\sigma_{CG}}{\sigma_{FG}}\right)^2\right] \ . \tag{21}$$

If the pileup of mixed dislocations (not only edge dislocations) is taken into account for a more realistic situation, $(1\text{-}\nu)/\mu$ in the above derivations is replaced by $2(1\text{-}\nu)/\mu(2\text{-}\nu)$. As a result, Eqs. (20) and (21), respectively, can be re-expressed as

$$N_{Hbar} = \frac{2\pi(1-\nu)kd_{FG}^{-1/2}}{M\mu(2-\nu)b}\left[1 - \left(\frac{\sigma_{CG}}{\sigma_{FG}}\right)^2\right] d_{CG} \tag{22}$$

and

$$\sigma_{tip} = \frac{2\pi(1-\nu)k^2 d_{CG}}{M\mu(2-\nu)bd_{FG}}\left[1 - \left(\frac{\sigma_{CG}}{\sigma_{FG}}\right)^2\right] \ . \tag{23}$$

Finally, the yield stress of these CGs against FGs, expressed as $\sigma_{CG,b}$ for the additional back stress strengthening, can be derived in form of Hall-Petch relation like Eq. (7):

$$\sigma_{CG,b} = \sigma_0 + \sqrt{\frac{M\mu(2-\nu)b\sigma_{tip}}{\pi(1-\nu)d_{CG}} + \sigma_{CG}^2}. \tag{24}$$

2.3. The yield strength of bimodal HGS

A polycrystalline material with a bimodal grain structure (FGs and CGs) is in turn to be considered in the following calculation for the global yield stress. FGs act as hard zones to constrain the soft zones before yielding, as illustrated in Fig. 4. The boundaries colored in red are interfaces between FGs and CGs. The schematic yield stress in Fig. 4, contributed from three kinds of grains, including regular FGs and CGs following Hall-Petch relation and special CGs additionally hardened by back stress, can be expressed using ROM as

$$\sigma_y = f_{FG}\sigma_{FG} + \left(f_{CG} - f_{CG,b}\right)\sigma_{CG} + f_{CG,b}\sigma_{CG,b} \tag{25}$$

where f_{FG} and f_{CG} are fractions of FGs and CGs, respectively, and $f_{CG,b}$ is the fraction of those CGs adjacent to FGs (yellow grains in Fig. 4). By substituting Eq. (24) into Eq. (25) coupled with quantitative measurements of microstructure, the theoretic yield stress of the bimodal HGS can be drawn.

3. Experimental methods

3.1. Materials

Bulk equiatomic CoCrNi (purity of each element > 99.9 at. %) was prepared by vacuum arc-melting at a Ti-gathered Ar atmosphere. All ingots were flipped and remelted at least five times to ensure the chemical homogeneity, and then the melt was dropped into a copper mold with a dimension of 5 × 10 × 150 mm^3. The as-cast alloys were homogenized at 1200℃ for 4 hours, and then water quenching. Next, cold rolling was conducted on the homogenized alloys along the longitudinal direction with a reduction of ~85%. Finally, the rolled sheets were sliced into proper sizes, and annealed in air at 700℃ for 1 hour, followed by water quenching for microstructural observations and mechanical tests. It is noted that the impact of short-range order was anticipated to be very weak or insignificant under such annealing condition (Zhang et al., 2020).

3.2. Microstructural analysis

Prior to microstructural observations, all specimens were first mechanically ground using SiC abrasive papers to 4000-grit, and

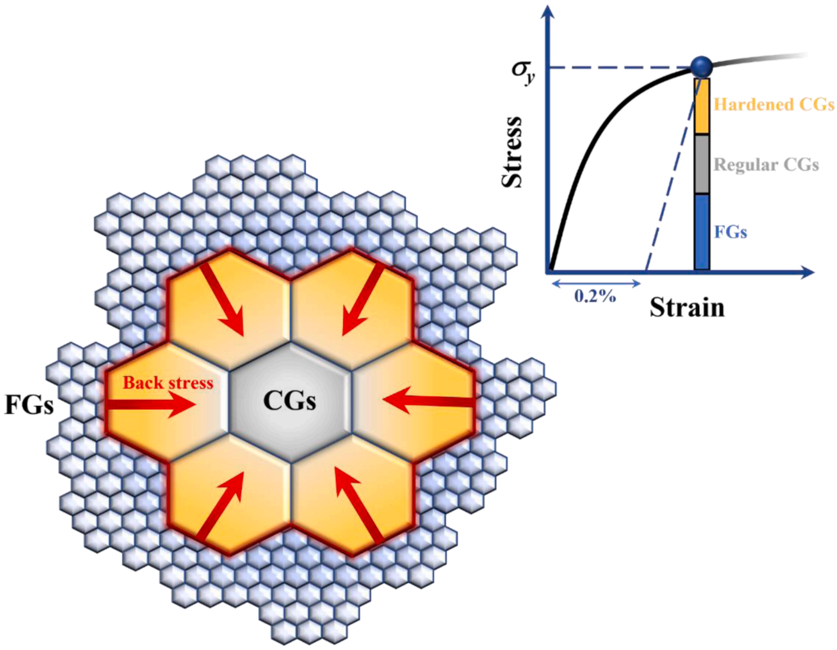

Fig. 4. Schematic illustration of HDI strengthening arising in the bimodal HGS upon yielding. The yield stress (σ_y), defined as 0.2% proof stress, comprises contributions from FGs, regular CGs, and hardened CGs, as indicated in the stress-strain curve (top right). With regards to the bimodal HGS, blue and grey grains represent FGs and CGs respectively, while yellow area refers to CGs additionally strengthened by the back stress of the interface.

then electropolished in a reagent of acetic acid, perchloric acid, and ethanol at 4℃ with a working voltage of 25 V. The phase identification was conducted using Bruker D2 phaser X-ray diffractometer (XRD). Zeiss Supra 55 scanning electron microscope (SEM) equipped with Oxford Instrument Symmetry S2 high-resolution electron backscatter diffraction (HR-EBSD) detector in conjunction of with the AztecHKL acquisition system was performed to quantitively examine the rolling direction-normal direction (RD-ND) surface of annealed specimens. The collected data were further post-processed by HKL Channel 5 software and MTEX toolbox in MATLAB.

3.3. Tensile testing

Dog-bone-shaped specimens were prepared by electro-discharge machining in a gauge dimension of $12.5 \times 3 \times \sim 1$ mm^3, in which longitudinal direction is parallel to rolling direction. After as-rolled tensile specimens were annealed at target temperatures, each face of the gauge section was mechanically polished using SiC abrasive papers to 4000-grit. The room temperature uniaxial tensile tests were carried out on Instron 3382 universal testing machine at a fixed initial strain rate of 1×10^{-3} s^{-1}, together with a 10-mm extensometer. LUR tensile tests were also performed to examine the HDI stress. For each cycling process, the specimens were reloaded until the force unloaded to 50 N, and the whole process was strain controlled at a fixed strain rate of 1×10^{-3} s^{-1}.

4. Result and discussion

4.1. Examination of the heterogeneous microstructure

According to our TMT results, a significant HGS is successfully achieved in the single-phase equimolar CoCrNi alloy by a heavy cold rolling with a reduction of 85% followed by the annealing treatment at 700℃ for 1 h (referred to as HGS-CoCrNi hereafter), as shown in Fig. 5(a). Several aggregates of CGs and FGs, respectively, are clearly revealed using EBSD with a low magnification of 250X and step size of 150 nm. These strips of CGs and FGs constrained each other to form a lamellar grain structure. Besides, the single FCC phase is verified by the XRD result in Fig. 5(b). To further quantitatively differentiate CG and FG zones, a higher magnification with a finer step

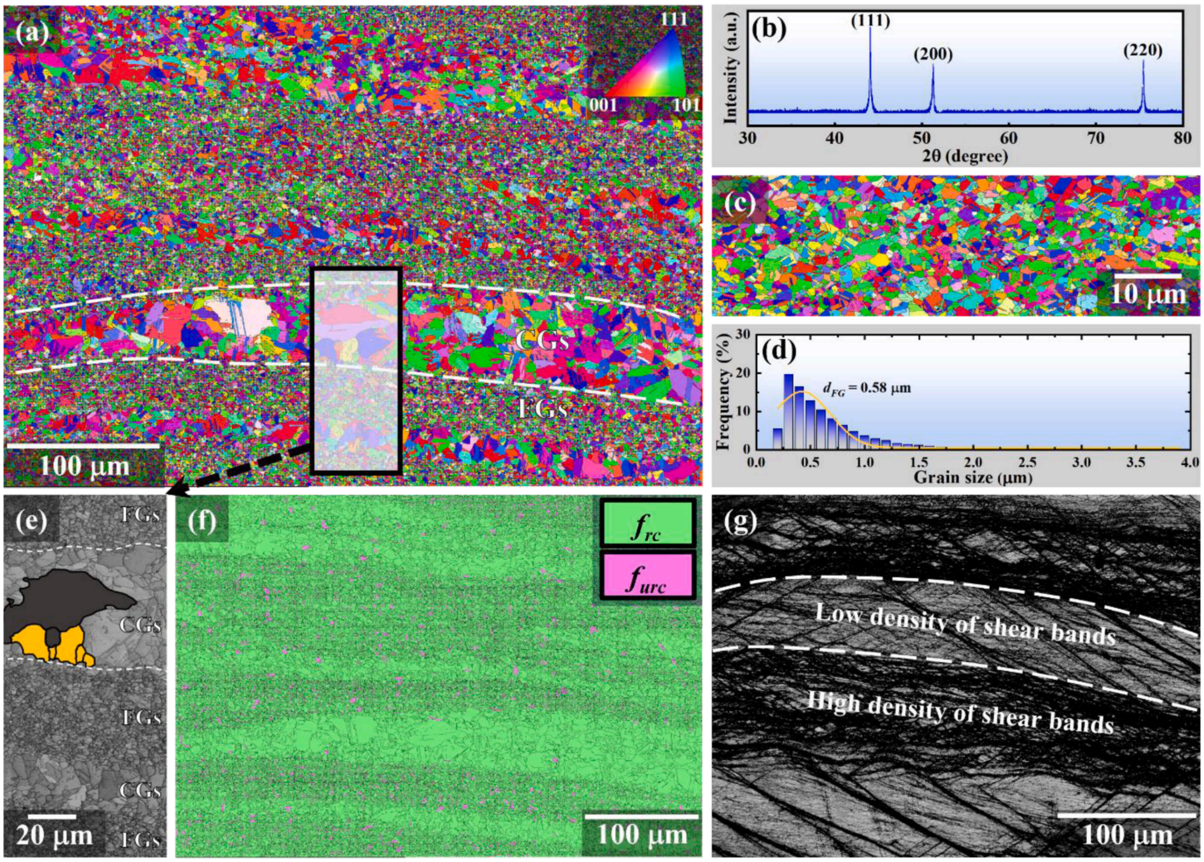

Fig. 5. (a) EBSD inverse pole figure along Z axis (IPF-Z) of as-rolled CoCrNi followed by annealing at 700℃ for 1 hour (HGS-CoCrNi). (b) XRD profile of HGS-CoCrNi. (c) Enlarged IPF-Z to examine the FG area in (a). (d) Statistics of grain size distribution in (c). (e) Enlarged band contrast image of (a) to representatively mark off regular CGs (colored in grey) and those CGs adjacent to the region of FGs. (f) Recrystallization map in the same place as (a). (g) Band contrast image of as-rolled sample.

size of 50 nm is employed to examine the FG region, as shown in Fig. 5(c). From the grain size analysis in Fig. 5(d), d_{FG} is statistically calculated as 0.58 μm, and the Gaussian-like distribution of grain size characterizes a homogeneous spread of FGs in Fig. 5(c). Since the largest grain size detected in Fig. 5(c) does not exceed 4 μm as shown in Fig. 5(d), it is reasonable to adopt the criterium of grain size ≥ 4 μm to compile statistics on CGs in Fig. 5(a). As a result, the average grain sizes and volume fractions are calculated as $d_{CG} = 6$ μm and $f_{CG} = 24\%$, as well as $d_{FG} = 0.58$ μm and $f_{FG} = 76\%$. To illustrate how to determine $f_{CG,b}$, the lamellar grain structure in Fig. 5(a) is partly enlarged, as shown in Fig. 5(e). Those CGs (colored in yellow) adjacent to the region of FGs with grain size < 4 μm are further distinguished from regular CGs (colored in grey), which gives $f_{CG,b} = 18\%$.

In our model, it is assumed that dislocations pile up in the strain-free CGs, i.e., recrystallized CGs, without the interference of pre-existing dislocations, so the distribution and fraction of recrystallization should be carefully evaluated. Due to no single definition made for recrystallization, there have been some strategies to determine recrystallized grains from different aspects of consideration. Among these, grain orientation spread (GOS) is a parameter to measure the long-range distribution of grain orientation, and the mechanism of primary recrystallization mostly relies on the grain boundary motion to eliminate such gradient orientation caused by pre-existing dislocations. Therefore, GOS could be the most relevant criterion to examine whether the microstructure in Fig. 5(a) meets our requirement. Here, we define recrystallized grains as those grains simultaneously fulfill two criteria recently proposed by Ayad *et al.* (Ayad et al., 2021): (i) GOS(i) < 2.5°; (ii) GOS(i)/d(i) < 1°/μm, where i is the grain number. Based on the above criteria, the distribution of recrystallization, included the fraction of recrystallized and unrecrystallized grains (f_{rc} and f_{urc}) is shown in Fig. 5(f). It is clear to see most CGs are almost recrystallized (colored in green in Fig. 5(f)), and $f_{rc} = 95\%$, suggesting a fully recrystallization is attained, which is ideal for our modeling. In addition, all quantitative parameters from EBSD data and literature are summarized in Table 1.

To understand the formation of HGS in Fig. 5(a), the deformation behavior of as-rolled sample is shown in Fig. 5(g). It reveals the inhomogeneous distribution of shear bands within the microstructure, which will not only affect the nucleation of recrystallization but also the recrystallized grain size (Koo and Yoon, 2001). The region with a lower density of shear bands, and thereby a lower stored energy, will tend to result in a larger grain size after primary recrystallization, while a finer grain size will be obtained in the more heavily deformed region with the presence of a high density of shear bands. Under a specific annealing temperature, the larger recrystallized grains may undergo secondary recrystallization at a higher growth rate to devour the surrounding fine recrystallized grains, which further promotes the discrete distribution of grain size (Thompson, 1985). After that, a large-scale HGS like Fig. 5(a) will form.

As reviewed before, several researchers conducted TMTs, similar to our design, on the equimolar CoCrNi alloy, but none of them reported an evident HGS resembling to Fig. 5(a). For example, Slone *et al.* (Slone et al., 2019) presented mostly equiaxial and recrystallized grains in the specimen subjected to cold rolling with a reduction of 70% and subsequent annealing at 700℃ for 1 hour. In the other work by Sathiyamoorthi *et al.* (Sathiyamoorthi et al., 2019), the cold-rolled sample with a reduction of 78% and subsequent annealing at 700℃ for 1 hour is also followed by a fully recrystallized microstructure with no prominent large grains. This difference may be due to the magnification and observing direction. If a high magnification is used, the scope of view will be too narrow to represent the whole feature, especially for studying the HS materials. Moreover, with regards to the effect of different observing directions, for instance, if the microstructure was inspected from the TD-RD direction in this research, it is possible to see only a layer of CGs or FGs because of the lamellar grain structure. Both influencing factors may make quantitative analysis unreliable. For example, inappropriate measurements of grain size could overestimate or underestimate the yield strength using the Hall-Petch equation.

4.2. Mechanical properties of HGS-CoCrNi

Uniaxial tensile testing was performed to investigate the mechanical properties of HGS-CoCrNi, as shown in Fig. 6(a). The alloy exhibits a σ_y, 0.2% proof stress, of 660 MPa, and reaches the ultimate tensile stress (σ_u) of 977 MPa with a uniform elongation (ε_u) of 37.4%, ended up with a total elongation (ε_t) of 47.4%.

Analysis: Conventional ROM

To probe the connection between σ_y and HGS, we decompose σ_y using conventional ROM below, considering FGs ($f_{FG} = 76\%$) and all CGs ($f_{CG} = 24\%$):

$$\sigma_y = f_{FG}\sigma_{FG} + f_{CG}\sigma_{CG} \tag{26}$$

Table 1
Summary of parameters from EBSD results and literature relevant to modeling.

Symbol	Physical meaning	Value
d_{CG}	Mean grain size of CGs	6 μm
d_{FG}	Mean grain size of FGs	0.58 μm
f_{CG}	Fraction of CGs	24%
f_{FG}	Fraction of FGs	76%
$f_{CG,b}$	Fraction of hardened CGs	18%
f_{rc}	Fraction of recrystallization	95%
σ_0	Friction stress	218 MPa (Yoshida et al., 2017)
$\sigma_{0,NG}$	Friction stress of nanograins	60 MPa (Yoshida et al., 2017)
k	Hall-Petch constant	265 MPa•μm$^{1/2}$ (Yoshida et al., 2017)
k_{NG}	Hall-Petch constant of nanograins	404 MPa•μm$^{1/2}$ (Yoshida et al., 2017)

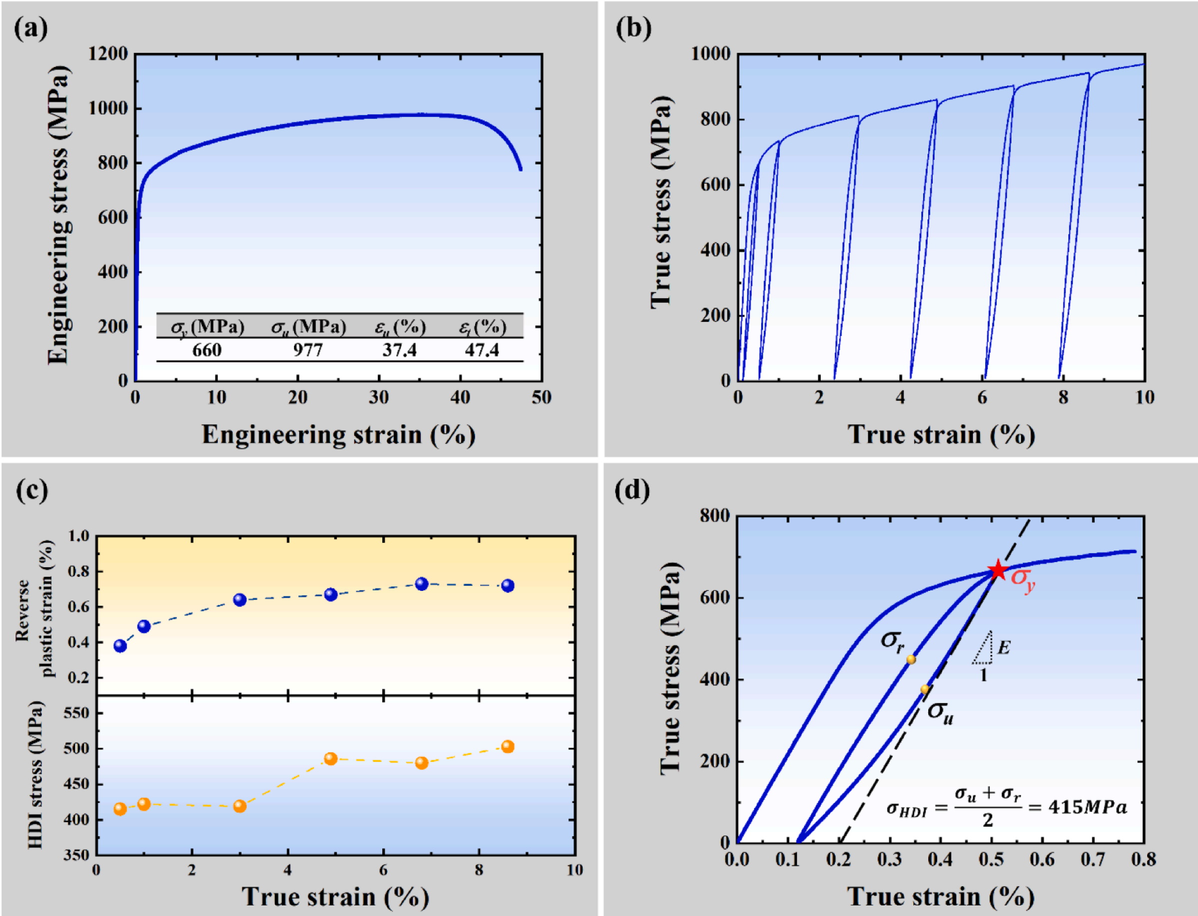

Fig. 6. Tensile testing of HGS-CoCrNi. (a) Engineering stress-strain curve. (b) Regular curve of LUR test including 6 cycles. (c) The amount of reverse plastic strain and HDI stress extracted from each cycle. (d) Partial enlargement of the first cycle in (b), unloading at nearly 0.2% proof stress.

where σ_{FG} and σ_{CG} can be estimated using the Hall-Petch equation (Eq. (1)). However, it should be noted that the extra-hardening phenomenon was observed in nanograins, making the Hall-Petch constant increase from its normal value (k) to that for nanograins (k_{NG}) (Yoshida et al., 2017), as listed in Table 1. Such a deviation will be considered in the calculation of σ_{FG} as well as the applied stress in Eq. (12) for modeling. Therefore,

$$\sigma_{CG} = \sigma_0 + kd_{CG}^{-1/2} = 326\ MPa \tag{27}$$

and

$$\sigma_{FG} = \sigma_{0,\ NG} + k_{NG}d_{FG}^{-1/2} = 590\ MPa \tag{28}$$

where all parameters have been well defined and also summarized in Table 1. Then substituting the values of σ_{CG} and σ_{FG}, with $f_{FG} =$ 76% and $f_{CG} = 24\%$, into Eq. (26) can derive a yield stress of 527 MPa, which is 133 MPa less than the experimental value (660 MPa) from Fig. 6(a). Apparently, it is proved that an additional HDI hardening must have acted to make up for this discrepancy that cannot be explained using ROM (Eq. (26)) solely.

Experimental verification: LUR testing

As a generally recognized method, the LUR test was conducted to inspect the influence of HDI strengthening, as shown in Fig. 6(b). It should be noted that deformation twinning, especially at high strains, was regarded as the origin of the extra strain hardening in CoCrNi MEA at room temperature due to the low SFE, 22 ± 4 mJ/m^2 from the experimental estimation (Laplanche et al., 2017) or even negative values from simulation (Huang et al., 2018). At a true strain of 9.7%, dislocations were found to glide on {111} planes and pile up against grain boundaries, indicating a significant slip planarity, while deformation twins appeared at the true strain up to 12.9% (Laplanche et al., 2017). Therefore, to exclude the contribution of twinning to HDI strengthening (De Cooman et al., 2018), six cyclic unloading-reloading tests were purposefully arranged within the true strain of 8.7% in the present study. For each cycle, the reverse plastic strain, the amount of displacement in true stain during unloading, and HDI stress, calculated according to the guidance from

Yang *et al.* (Yang et al., 2016a). are recorded in Fig. 6(c). It can be clearly seen that the hysteresis loops in Fig. 6(b)Fig. 6(b) are more obvious with increasing strain, which agrees with the upward tendency to reverse plastic strain shown in Fig. 6(c). Meanwhile, the prominent hysteresis loop also suggests a strong Bauschinger effect and further reflect in the ascending trend of HDI stress (Wu et al., 2015). As expected, LUR results indicate the existence of typical HDI hardening stemming from HGS.

To more precisely evaluate the contribution of HDI stress to yield stress, the first unloading point is deliberately arranged at the true strain of 0.5%, which is close to 0.2 proof stress, as shown in Fig. 6(d). The labeled unloading yield stress (σ_{uy}) and reloading yield stress (σ_{ry}) correspond to the location of 5% slope reduction from effective Young's modulus (E), as suggested by Yang *et al.* (Yang et al., 2016a). Thus, σ_{HDI} can be calculated using

$$\sigma_{HDI} = \frac{\sigma_{uy} + \sigma_{ry}}{2} \tag{29}$$

and the yield stress is

$$\sigma_y = \sigma_e + \sigma_{HDI} \tag{30}$$

where σ_e is the effective stress, mostly from σ_0 (218 MPa) in our case. Substituting all known values of parameters into Eqs. (29) and (30) produces a yield stress of 633 MPa, which is reasonable to the observed yield stress (660 MPa). Compared to the serious underestimation of yield stress using conventional ROM (Eq. (26)), the LUR test can well explain HDI strengthening from an experimental perspective. These results indicate the necessity to develop another model for accurately predicting the yield stress in the presence of HDI strengthening. This will be addressed in following discussions.

4.3. Integration of modeling and experimental results

On the quantitative comparison of l_{Hbar}

Researches on HS materials have all ascribed the superior mechanical properties to the presence of pileups in l_{Hbar}, but few efforts are taken to formulate the relationship between microstructure and mechanical properties in detail. Ma *et al.* (Ma et al., 2016) firstly conducted a systematic study on the role of interfaces played in the copper/bronze laminates fabricated by accumulative roll bonding. According to their GND statistics via EBSD, l_{Hbar} is very close to 5 µm, the grain size of copper (soft zone). Later Huang *et al.* (Huang et al., 2018) adopted the same material and expressed l_{Hbar} as

$$l_{Hbar} \approx \left(\frac{\mu}{\sigma_y}\right) b \ . \tag{31}$$

However, because σ_y is unknown unless the tensile test is carried out, this equation could only be a reference to experimental results. Furthermore, despite some parameters simplified through assumptions, Eq. (31) involves no HDI characteristics, which makes it not specific to HS materials. In this work, the modified model addresses these inadequacies, taking HGS-CoCrNi and copper/bronze laminates (Ma et al., 2016) as examples in the calculation below.

Substituting derived values of HGS-CoCrNi into Eq. (19) yields:

$$l_{Hbar} = \left[1 - \left(\frac{\sigma_{CG}}{\sigma_{FG}}\right)^2\right] d_{CG} = 0.7 d_{CG} = 4.2\ \mu m \tag{32}$$

This shows how our model predicts a relationship between Hbar and the grain size of the soft zone, $l_{Hbar} = 0.7 d_{CG}$ in HGS-CoCrNi, which mechanism leads to the difference in strength between these two zones. From the above equation, it can be seen that l_{Hbar} will increase with increasing the difference between σ_{FG} and σ_{CG} until approach to d_{CG}, for situations like $\sigma_{FG} = 4\sigma_{CG}$. Surprisingly, by additionally referring to literature (Pande and Cooper, 2009; Zaynullina et al., 2018), the strength of bronze is approximately four times higher than that of copper in copper/bronze laminates (Ma et al., 2016), giving $l_{Hbar} \sim d_{CG}$, as Eq. (19) predicted. To further validate the predicted l_{Hbar} at yield point, more in-situ observations, such as transmission electron microscopy (TEM), EBSD, and micro-digital image correlation (Huang et al., 2018; Park et al., 2018), are expected to be conducted on other HS materials.

On the quantitative comparison of σ_y

As mentioned before, Eqs. (22) and (23) should be rewritten in consideration of k_{NG}. Accordingly,

$$N_{Hbar} = \frac{2\pi(1-\nu) k_{NG} d_{FG}^{-1/2}}{M\mu(2-\nu) b} l_{Hbar} \tag{33}$$

and

$$\sigma_{tip} = \frac{2\pi(1-\nu) k_{NG}^2}{M\mu(2-\nu) b d_{FG}} l_{Hbar} \tag{34}$$

By mimicking the derivation of Eq. (24) and substituting known variables, the yield stress of back stress strengthened CG can be reduced to

$$\sigma_{CG,b} = \sigma_0 + \sqrt{\frac{2k_{NG}^2}{d_{CG}d_{FG}} l_{IAZ} + \sigma_{CG}^2} = 925\ MPa\ . \tag{35}$$

This value can be possible, since it does not exceed σ_{uy}, the maximum hardening capacity in HGS-CoCrNi, as shown in Fig. 6(a). In addition, a large strain gradient near the interface is revealed in Huang *et al.*'s observations (Huang et al., 2018), which suggests Hbar can effectively accommodate more dislocation pileups than either FGs or CGs can, causing more profound hardening, as illustrated in Fig. 7. As stated in model development, the tip stress acting on the interface is the same with that on the grain boundary of FG, like action-reaction force pairs, so the dislocation densities at these two pileup heads should be identical and higher than that at the grain boundary of CG. But the boundary condition of d_{FG} limits the accumulation of dislocations in FG. In contrast, the relation of $l_{Hbar} \sim d_{CG}$ allows more dislocations within Hbar, as represented by the yellow area in Fig. 7. This is the reason why $\sigma_{CG,b}$ could be higher than σ_{CG}.

Finally, by substituting $\sigma_{CG,b}$ as well as other known values of parameters into Eqs. (25), the predicted σ_y from modeling is given:

$$\sigma_y = f_{FG}\sigma_{FG} + (f_{CG} - f_{CG,b})\sigma_{CG} + f_{CG,b}\sigma_{CG,b} = 635\ MPa \tag{36}$$

Compared with ROM and LUR testing, our model successfully predicts a value of 635 MPa close to the actual yield stress, as listed in Table 2.

Above fitting results amend the inadequacy of conventional ROM using the Hall-Petch equation, and theoretically supplements HDI strengthening mechanism. Instead of a complex combination of parameters, physical quantities, e.g., l_{Hbar} and $\sigma_{CG,b}$, can be simplified in a handy form of Eq. (32) and (35), respectively, but HDI characteristics like d_{CG} of soft zone and d_{FG} of hard zone still remain. In both Eqs. (32) and (35), it is clear to see how the calculated values are affected by these characteristics solved by microstructural characterizations and the Hall-Petch relation. Understanding the proportional relationship between σ_{CG} and σ_{FG}, one is able to tailor the mechanical property of HGS as well as other HS materials.

5. Conclusion

In this research, we have proposed a theoretical model to parameterize the HDI strengthening effect, then validated it by our own experiment on a single-phase HGS. The key achievements and statements are:

(1) The model based on classic single-ended dislocation pileup theory was concisely expressed, including several HDI characteristics. Once the grain sizes, Hall-Petch constants, and fractions of hard and soft zones, respectively, have been determined, the width of Hbar and HDI stress upon yielding can be estimated accordingly.
(2) Two zones with a significant difference in grain size were produced in the equimolar single-phase CoCrNi MEA as a representative of heterogeneous grain structure. Such microstructure could be easily ignored by experimental artifacts so that the measured grain size may not properly reflect the expected yield stress using the Hall-Petch equation.
(3) The width of Hbar, dependent on the difference in strengths between soft and hard zones, approximately equals to the mean grain size of soft zone only if the theoretical yield stress of hard zone is four times higher than that of the soft zone, which successfully explained previous experimental observations (Ma et al., 2016).
(4) Compared to conventional ROM, our model successfully predicted the yield stress of a bimodal HGS, which agreed well with the LUR results. The fitting result suggested that the yield stress of the coarse grains strengthened by the dislocations pileups against the interface was effectively increased.
(5) This model is anticipated to not only estimate the yield strength of HS materials but also serve as a guide to tailor heterogeneous microstructures for maximizing HDI strengthening. Based on this development, more efforts will be put into expressing HDI strain hardening in consideration of forward stress and back stress.

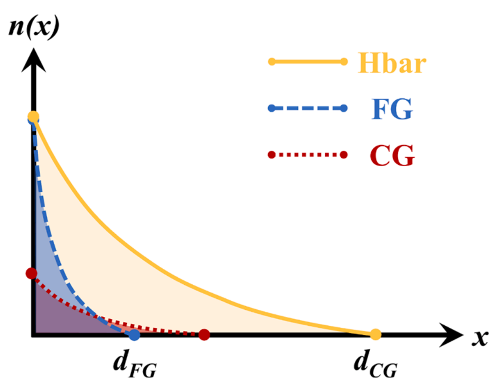

Fig. 7. Schematic illustration of the dislocation densities at yielding, in Hbar, FG, and CG respectively, plotted against the distance from the interface or grain boundary.

Table 2
Estimated σ_y of HGS-CoCrNi from different methods.

Tensile testing	ROM	LUR testing	Our model
660 MPa	527 MPa	633 MPa	635 MPa

CRediT authorship contribution statement

T.H. Chou: Conceptualization, Methodology, Investigation, Validation, Writing – original draft, Writing – review & editing. **W.P. Li:** Conceptualization, Methodology, Investigation, Writing – review & editing. **H.W. Chang:** Investigation. **X.H. Du:** Investigation, Resources. **W.S. Chuang:** Conceptualization, Writing – review & editing. **T. Yang:** Writing – review & editing, Supervision, Funding acquisition. **Y.T. Zhu:** Writing – review & editing. **J.C. Huang:** Conceptualization, Writing – review & editing, Supervision, Funding acquisition.

Declaration of Competing Interest

Authors declare no conflict of interest.

Data Availability

No data was used for the research described in the article.

Acknowledgment

The authors gratefully acknowledge the sponsorship from City University of Hong Kong under Grant No. 21205621, 9380088, 9360157, 9360161, and 7005078. T. Yang also thanks to the financial support from the Shenzhen Science and Technology Program (Grant No. SGDX20210823104002016).

Reference

Ayad, A., Ramoul, M., Rollett, A., Wagner, F., 2021. Quantifying primary recrystallization from EBSD maps of partially recrystallized states of an IF steel. Mater. Charact. 171, 110773.
Bouaziz, O., Moon, J., Kim, H.S., Estrin, Y., 2021. Isotropic and kinematic hardening of a high entropy alloy. Scr. Mater. 191, 107–110.
Cottrell, A.H., Bilby, B.A., 1949. Dislocation theory of yielding and strain ageing of iron. Proc. Phys. Soc. London Sect. A 62, 49.
De Cooman, B.C., Estrin, Y., Kim, S.K., 2018. Twinning-induced plasticity (TWIP) steels. Acta Mater. 142, 283–362.
Eshelby, J., 1949. LXXXII. Edge dislocations in anisotropic materials. London, Edinburgh, Dublin Philosoph. Mag. J. Sci. 40, 903–912.
Eshelby, J., Frank, F., Nabarro, F., 1951. XLI. The equilibrium of linear arrays of dislocations. London, Edinburgh, Dublin Philosoph. Mag. J. Sci. 42, 351–364.
Fan, J., Ji, X., Fu, L., Wang, J., Ma, S., Sun, Y., Wen, M., Shan, A., 2022. Achieving exceptional strength-ductility synergy in a complex-concentrated alloy via architected heterogeneous grains and nano-sized precipitates. Int. J. Plast., 103398
Friedman, L.H., Chrzan, D., 1998. Continuum analysis of dislocation pile-ups: influence of sources. Philos. Mag. A 77, 1185–1204.
Gao, B., Chen, X., Pan, Z., Li, J., Ma, Y., Cao, Y., Liu, M., Lai, Q., Xiao, L., Zhou, H., 2019. A high-strength heterogeneous structural dual-phase steel. J. Mater. Sci. 54, 12898–12910.
Gao, J., Nutter, J., Liu, X., Guan, D., Huang, Y., Dye, D., Rainforth, W.M., 2018. Segregation mediated heterogeneous structure in a metastable β titanium alloy with a superior combination of strength and ductility. Sci. Rep. 8, 1–11.
Hasan, M., Liu, Y., An, X., Gu, J., Song, M., Cao, Y., Li, Y., Zhu, Y., Liao, X., 2019. Simultaneously enhancing strength and ductility of a high-entropy alloy via gradient hierarchical microstructures. Int. J. Plast. 123, 178–195.
Hall, E., 1951. The deformation and ageing of mild steel: III discussion of results. Proc. Phys. Soc. London Sect. B 64, 747.
He, F., Yang, Z., Liu, S., Chen, D., Lin, W., Yang, T., Wei, D., Wang, Z., Wang, J., Kai, J.-j., 2021. Strain partitioning enables excellent tensile ductility in precipitated heterogeneous high-entropy alloys with gigapascal yield strength. Int. J. Plast. 144, 103022.
He, Z., Jia, N., Yan, H., Shen, Y., Zhu, M., Guan, X., Zhao, X., Jin, S., Sha, G., Zhu, Y., 2021. Multi-heterostructure and mechanical properties of N-doped FeMnCoCr high entropy alloy. Int. J. Plast. 139, 102965.
Head, A., Louat, N., 1955. The distribution of dislocations in linear arrays. Aust. J. Phys. 8, 1–7.
Hirth, J.P., Lothe, J., Mura, T., 1983. Theory of dislocations. J. Appl. Mech. 50, 476.
Huang, C., Wang, Y., Ma, X., Yin, S., Höppel, H., Göken, M., Wu, X., Gao, H., Zhu, Y., 2018. Interface affected zone for optimal strength and ductility in heterogeneous laminate. Mater. Today 21, 713–719.
Huang, H., Li, X., Dong, Z., Li, W., Huang, S., Meng, D., Lai, X., Liu, T., Zhu, S., Vitos, L., 2018. Critical stress for twinning nucleation in CrCoNi-based medium and high entropy alloys. Acta Mater. 149, 388–396.
Kim, J.G., Jang, M.J., Park, H.K., Chin, K.-G., Lee, S., Kim, H.S., 2019. Back-stress effect on the mechanical strength of TWIP-IF steels layered sheet. Met. Mater. Int. 25, 912–917.
Koo, J.B., Yoon, D.Y., 2001. Abnormal grain growth in bulk Cu—The dependence on initial grain size and annealing temperature. Metall. Mater. Trans. A 32, 1911–1926.
Lai, Z., Mai, Y., Song, H., Mai, J., Jie, X., 2022. Heterogeneous microstructure enables a synergy of strength, ductility and electrical conductivity in copper alloys. J. Alloys Compd. 902, 163646.
Laplanche, G., Kostka, A., Reinhart, C., Hunfeld, J., Eggeler, G., George, E., 2017. Reasons for the superior mechanical properties of medium-entropy CrCoNi compared to high-entropy CrMnFeCoNi. Acta Mater. 128, 292–303.
Leibfried, G., 1951. Verteilung von Versetzungen im statischen Gleichgewicht. Zeitschrift für Physik 130, 214–226.
Li, J., Chou, Y., 1970. The role of dislocations in the flow stress grain size relationships. Metallur. Materials Trans. B 1, 1145–1159.
Li, J., Lu, W., Gibson, J., Zhang, S., Korte-Kerzel, S., Raabe, D., 2020. Compatible deformation and extra strengthening by heterogeneous nanolayer composites. Scr. Mater. 179, 30–35.

Li, W., Chou, T.-H., Yang, T., Chuang, W.-S., Huang, J.C., Luan, J., Zhang, X., Huo, X., Kong, H., He, Q., 2021. Design of ultrastrong but ductile medium-entropy alloy with controlled precipitations and heterogeneous grain structures. Appl. Mater. Today 23, 101037.

Liu, S., Xia, D., Yang, H., Huang, G., Yang, F., Chen, X., Tang, A., Jiang, B., Pan, F., 2022. Mechanical properties and deformation mechanism in Mg-Gd alloy laminate with dual-heterostructure grain size and texture. Int. J. Plast., 103371

Lu, K., 2014. Making strong nanomaterials ductile with gradients. Science 345, 1455–1456.

Lu, W., Luo, X., Yang, Y., Huang, B., 2020. Hall-petch relationship and heterogeneous strength of CrCoNi medium-entropy alloy. Mater. Chem. Phys. 251, 123073.

Ma, X., Huang, C., Moering, J., Ruppert, M., Höppel, H.W., Göken, M., Narayan, J., Zhu, Y., 2016. Mechanical properties of copper/bronze laminates: Role of interfaces. Acta Mater. 116, 43–52.

Misra, A., Göken, M., Mara, N.A., Beyerlein, I.J., 2021. Hierarchical and heterogeneous multiphase metallic nanomaterials and laminates. MRS Bull. 46, 236–243.

Mott, N.F., 1952. CXVII. A theory of work-hardening of metal crystals. London, Edinburgh, Dublin Philosoph. Mag. J. Sci. 43, 1151–1178.

Murr, L., 2016. Dislocation ledge sources: dispelling the myth of Frank–Read source importance. Metall. Mater. Trans. A 47, 5811–5826.

Niu, G., Zurob, H.S., Misra, R., Tang, Q., Zhang, Z., Nguyen, M.-T., Wang, L., Wu, H., Zou, Y., 2022. Superior fracture toughness in a high-strength austenitic steel with heterogeneous lamellar microstructure. Acta Mater. 226, 117642.

Pande, C., Cooper, K., 2009. Nanomechanics of Hall–Petch relationship in nanocrystalline materials. Prog. Mater Sci. 54, 689–706.

Park, H.K., Ameyama, K., Yoo, J., Hwang, H., Kim, H.S., 2018. Additional hardening in harmonic structured materials by strain partitioning and back stress. Mater. Res. Lett. 6, 261–267.

Park, J.M., Yang, D.C., Kim, H.-J., Kim, D.G., Lee, S., Kim, H.S., Sohn, S.S., 2021. Ultra-strong and strain-hardenable ultrafine-grained medium-entropy alloy via enhanced grain-boundary strengthening. Mater. Res. Lett. 9, 315–321.

Petch, N., 1953. The cleavage strength of polycrystals. J. Iron Steel Inst. 174, 25–28.

Sathiyamoorthi, P., Asghari-Rad, P., Bae, J.W., Kim, H.S., 2019. Fine tuning of tensile properties in CrCoNi medium entropy alloy through cold rolling and annealing. Intermetallics 113, 106578.

Sathiyamoorthi, P., Bae, J.W., Asghari-Rad, P., Park, J.M., Kim, J.G., Kim, H.S., 2018. Effect of annealing on microstructure and tensile behavior of CoCrNi medium entropy alloy processed by high-pressure torsion. Entropy 20, 849.

Sathiyamoorthi, P., Kim, H.S., 2022. High-entropy alloys with heterogeneous microstructure: processing and mechanical properties. Prog. Mater Sci. 123, 100709.

Sawangrat, C., Kato, S., Orlov, D., Ameyama, K., 2014. Harmonic-structured copper: performance and proof of fabrication concept based on severe plastic deformation of powders. J. Mater. Sci. 49, 6579–6585.

Shin, S., Zhu, C., Zhang, C., Vecchio, K.S., 2019. Extraordinary strength-ductility synergy in a heterogeneous-structured β-Ti alloy through microstructural optimization. Mater. Res. Lett. 7, 467–473.

Shukla, S., Choudhuri, D., Wang, T., Liu, K., Wheeler, R., Williams, S., Gwalani, B., Mishra, R.S., 2018. Hierarchical features infused heterogeneous grain structure for extraordinary strength-ductility synergy. Mater. Res. Lett. 6, 676–682.

Slone, C., Miao, J., George, E.P., Mills, M.J., 2019. Achieving ultra-high strength and ductility in equiatomic CrCoNi with partially recrystallized microstructures. Acta Mater. 165, 496–507.

Thompson, C., 1985. Secondary grain growth in thin films of semiconductors: theoretical aspects. J. Appl. Phys. 58, 763–772.

Wang, Y., Chen, M., Zhou, F., Ma, E., 2002. High tensile ductility in a nanostructured metal. Nature 419, 912–915.

Wang, Y., Huang, C., Li, Y., Guo, F., He, Q., Wang, M., Wu, X., Scattergood, R.O., Zhu, Y., 2020. Dense dispersed shear bands in gradient-structured Ni. Int. J. Plast. 124, 186–198.

Wang, Y., Wang, M., Fang, X., Guo, F., Liu, H., Scattergood, R., Huang, C., Zhu, Y., 2019. Extra strengthening in a coarse/ultrafine grained laminate: Role of gradient interfaces. Int. J. Plast. 123, 196–207.

Wang, Y., Yang, M., Ma, X., Wang, M., Yin, K., Huang, A., Huang, C., 2018. Improved back stress and synergetic strain hardening in coarse-grain/nanostructure laminates. Mater. Sci. Eng. 727, 113–118.

Wu, H., Fan, G., 2020. An overview of tailoring strain delocalization for strength-ductility synergy. Prog. Mater Sci. 113, 100675.

Wu, S., Wang, G., Wang, Q., Jia, Y., Yi, J., Zhai, Q., Liu, J., Sun, B., Chu, H., Shen, J., 2019. Enhancement of strength-ductility trade-off in a high-entropy alloy through a heterogeneous structure. Acta Mater. 165, 444–458.

Wu, X., Jiang, P., Chen, L., Zhang, J., Yuan, F., Zhu, Y., 2014. Synergetic strengthening by gradient structure. Mater. Res. Lett. 2, 185–191.

Wu, X., Yang, M., Yuan, F., Wu, G., Wei, Y., Huang, X., Zhu, Y., 2015. Heterogeneous lamella structure unites ultrafine-grain strength with coarse-grain ductility. Proc. Natl Acad. Sci. 112, 14501–14505.

Xiong, T., Zheng, S., Pang, J., Ma, X., 2020. High-strength and high-ductility AlCoCrFeNi2. 1 eutectic high-entropy alloy achieved via precipitation strengthening in a heterogeneous structure. Scr. Mater. 186, 336–340.

Yang, M., Pan, Y., Yuan, F., Zhu, Y., Wu, X., 2016a. Back stress strengthening and strain hardening in gradient structure. Mater. Res. Lett. 4, 145–151.

Yang, M., Yan, D., Yuan, F., Jiang, P., Ma, E., Wu, X., 2018. Dynamically reinforced heterogeneous grain structure prolongs ductility in a medium-entropy alloy with gigapascal yield strength. Proc. Natl Acad. Sci. 115, 7224–7229.

Yang, M., Yuan, F., Xie, Q., Wang, Y., Ma, E., Wu, X., 2016b. Strain hardening in Fe–16Mn–10Al–0.86 C–5Ni high specific strength steel. Acta Mater. 109, 213–222.

Yoshida, S., Bhattacharjee, T., Bai, Y., Tsuji, N., 2017. Friction stress and Hall-Petch relationship in CoCrNi equi-atomic medium entropy alloy processed by severe plastic deformation and subsequent annealing. Scr. Mater. 134, 33–36.

Zaynullina, L., Sitdikov, V., Alexandrov, I., Wei, W., 2018. In: Effect of SPD on the Structure Formation and Mechanical Properties of the Cu-10% Zn alloy, IOP Conference Series: Materials Science and Engineering. IOP Publishing, 012041.

Zhang, C., Bao, X., Zhang, D., Chen, W., Zhang, J., Kuang, J., Liu, G., Sun, J., 2021. Achieving superior strength-ductility balance in a novel heterostructured strong metastable β-Ti alloy. Int. J. Plast. 147, 103126.

Zhang, C., Zhu, C., Vecchio, K., 2019. Non-equiatomic FeNiCoAl-based high entropy alloys with multiscale heterogeneous lamella structure for strength and ductility. Mater. Sci. Eng. 743, 361–371.

Zhang, R., Zhao, S., Ding, J., Chong, Y., Jia, T., Ophus, C., Asta, M., Ritchie, R.O., Minor, A.M., 2020. Short-range order and its impact on the CrCoNi medium-entropy alloy. Nature 581, 283–287.

Zhang, Z., Vajpai, S.K., Orlov, D., Ameyama, K., 2014. Improvement of mechanical properties in SUS304L steel through the control of bimodal microstructure characteristics. Mater. Sci. Eng. 598, 106–113.

Zhong, S., Xu, C., Li, Y., Li, W., Luo, H., Peng, R., Jia, X., 2022. Hierarchy modification induced exceptional cryogenic strength, ductility and toughness combinations in an asymmetrical-rolled heterogeneous-grained high manganese steel. Int. J. Plast. 154, 103316.

Zhu, Y., Ameyama, K., Anderson, P.M., Beyerlein, I.J., Gao, H., Kim, H.S., Lavernia, E., Mathaudhu, S., Mughrabi, H., Ritchie, R.O., 2021. Heterostructured materials: superior properties from hetero-zone interaction. Mater. Res. Lett. 9, 1–31.

Zhu, Y., Wu, X., 2019. Perspective on hetero-deformation induced (HDI) hardening and back stress. Mater. Res. Lett. 7, 393–398.

Zou, Y., Ding, H., Zhang, Y., Tang, Z., 2022. Microstructural evolution and strain hardening behavior of a novel two-stage warm rolled ultra-high strength medium Mn steel with heterogeneous structures. Int. J. Plast. 151, 103212.